Aeroacoustics Conferences
30 May - 1 June, 2016, Lyon, France
22nd AIAA/CEAS Aeroacoustics Conference

10.2514/6.2016-2743

A preliminary semi-analytical approach for CROR noise modeling

Michael E. Quaglia,* Stephane Moreau†
Université de Sherbrooke,
Sherbrooke, J1K2R1, QC, Canada
Michel Roger,‡
Ecole Centrale de Lyon, centre acoustique
Ecully, France
Rasika Fernando§
Safran Snecma, Aerodynamics and Acoustics Department,
77550 Moissy-Cramayel, France

April 14, 2016

A preliminary approach for semi-analytical CROR noise modeling is investigated. The velocity inputs extracted from URANS simulations are used in order to compute both tonal and broadband noise contributions of a realistic CROR geometry. For the moment the tonal part includes an Orthogonal Blade-Vortex Interaction (OBVI) model based on the work performed by Quaglia *et al.*[1] using a frequency-based rotating dipole formulation of the FWH equation. The broadband part includes the Broadband Rotor-Wake Interaction (BRWI) model developed by Blandeau *et al.*[2] For the tonal part, the directivities of the OBVI model are fairly predicted in the forward arc. However, both the directivities and levels of the backward arc are not predicted. This may comes from a misprediction of the tip effect in the acoustic source evaluation. Better results are obtained using the Mean Camber Surface (MCS)[3] instead of a classical flat plate for acoustic propagation. Concerning the broadband model, the BRWI noise is shown to be tip driven. A problem is encountered also at the tip for the evaluation of the half-wake size. This is due to the presence of the tip-vortex which does not behave like a viscous wake. Thus, the modulation function used in the BRWI model needs investigation in order to accurately describe the particular case of Broadband Rotor-Vortex interaction (BRVI).

Nomenclature

b_φ	lead of the vortex helicoidal path
c_β	Contraction radius coefficient linked to β
G	Upwash spectral density, [m^2]
k	Turbulent kinetic energy, [m^{2}s^{-2}]
(k_x, k_y)	aft-blade chordwise and spanwise wanumbers [1/m]
(k'_x, k'_y)	aft-blade chordwise and spanwise wanumbers with sweep [1/m]
$k_{x,m}$	Wavenumber of the mth harmonic loading, [1/m]
L_w	Half-wake size, [m]
M_X	Axial Mach number
m, n	Loading (front rotor) and sound (aft rotor) indexes

*Ph.D candidate, Mechanical Engineering Department, michael.quaglia@usherbrooke.ca
†Professor, Mechanical Engineering Department, stephane.moreau@usherbrooke.ca, AIAA Lifetime Member
‡Professor, Acoustic Department, michel.roger@ec-lyon.fr
§Doctor Engineer, Acoustics Department, rasika.fernando@snecma.fr

r_0	Vortex core radius, [m]
R_{BVI}	Radial locus of the BVI event, [m]
R_1, R_2	Front and aft rotor
U_c	Phase velocity AND relative flow speed, [m/s]
u_{rms}	Root mean square of the turbulent velocity, [m/s]
w	Upwash velocity, (velocity component in the y_3 direction at $y_3 = 0$), [m/s]
$[X_v, Y_v, Z_v]$	Trajectory of the vortex core, [m,m,m]
α_β	Vena contracta rate
α	Lamb-Oseen coefficient V^{max} at $r/r_0 = 1$
β	Vena contracta angle, [rad]
Γ	Incomplete upper Gamma function
$\Delta\tilde{p}$	Spectral local pressure jump, [kg m^{-1} s^{-1}]
χ_1, χ_2	Blade stagger angle front and rear rotor defined from the rotational axis, [rad]
Λ	Integral length scale, [m]
$\Phi_{ww}^{(2)}$	2D Turbulent velocity spectrum
Ψ	Local Sweep angle, [rad]
φ	Front-rotor tip vortex helicity angle, [rad]
γ_1, γ_2	Blade stagger angle front and rear rotor defined from the rotational plane, [rad]
Σ	Integral length scale of the incoming turbulence, [m]
Ω_1, Ω_2	Rotational speed for the front and aft rotor respectively, [rad/s]
ω	Specific dissipation rate, [1/s]
ω_s	Acoustic pulsation, [rad/s]
Subscript	
chord	Coefficient relative to the rear rotor chord (x_{c2})
span	Coefficient relative to the rear rotor chord (y_{c2})
Superscript	
$*$	Dimensionless distance and wavenumber for the loading part
LO	Lamb-Oseen vortex
Sc	Scully vortex
Ta	Taylor vortex

I. Introduction

Because of the weight and space limitation of nacelles for turbofans, Counter-Rotating Open Rotor (*CROR*) design is a viable alternative to classical turboengines for commercial airplane propulsion. Since the beginning of CROR design with the preliminary work on the UnDucted Fan engine in the mid-eighties,[4] significant tonal noise reduction for this novel architecture has been achieved. Nowadays, 3D aerodynamic and aeroacoustic optimization have yielded fully three-dimensional blade shapes and cropped aft rotor that have achieved substantial reductions in tonal noise.[5,6,7]

The present issue is that 3D aerodynamics still take some time to compute and are particularly slow for geometrical optimization. In a view to quickly assess preliminary geometries, analytical models are being used. A preliminary investigation of both tonal and broadband noise evaluation is being developed in the current work.

Because analytical modeling implies some geometrical and flow assumptions and because it is not yet realistic to model every noise source for CROR configurations, the complete methodology is drawn in the next part of this paper. It is followed by a detailed description of each tonal and broadband model used in the current approach. Thereafter, results are given for each model and compared with fully numerical solutions and other semi-analytical approaches when possible. Finally, a conclusion is drawn about the current tool and the next steps of the modeling.

II. Methodology

For CROR geometries at approach or take-off operating conditions, interaction noise is the fundamental noise source[8] and is related to the impingement of velocity fluctuations shed by surfaces. These velocity

fluctuations create an unsteady loading on the impinged rotor, the acoustic sources. These noise sources will thereafter radiate noise.

In order to assess the noise it is thus fundamental to breakdown every possible velocity fluctuation produced by CROR configurations. Figure 1 shows a preliminary complete breakdown based on literature. From an acoustic point of view, the velocity fluctuations are split in two main categories, deterministic and turbulent fluctuations.

On the one hand, Figure 1a represents the deterministic velocity fluctuations induced by the blades of the rotors. They radiate at discrete frequencies, called interaction tones. For CROR, because of the counter-rotating motion, interaction tones radiate at frequencies given by linear combination of each rotor Blade Passing Frequency (BPF) and their higher harmonics:

$$mBPF_1 + nBPF_2 \qquad (m,n) \in \mathbb{Z}^2, \tag{1}$$

with the subscripts 1 and 2 representing the front (R_1) and aft (R_2) rotor respectively.

On the other hand, Figure 1b shows the turbulent velocity fluctuations. Contrary to deterministic velocity fluctuations the latter will radiate at all frequencies. Despite the fact that tones are the main contributors of the overall noise for CROR configurations, third-octave sound power levels showed the importance of broadband noise for CROR.[9]

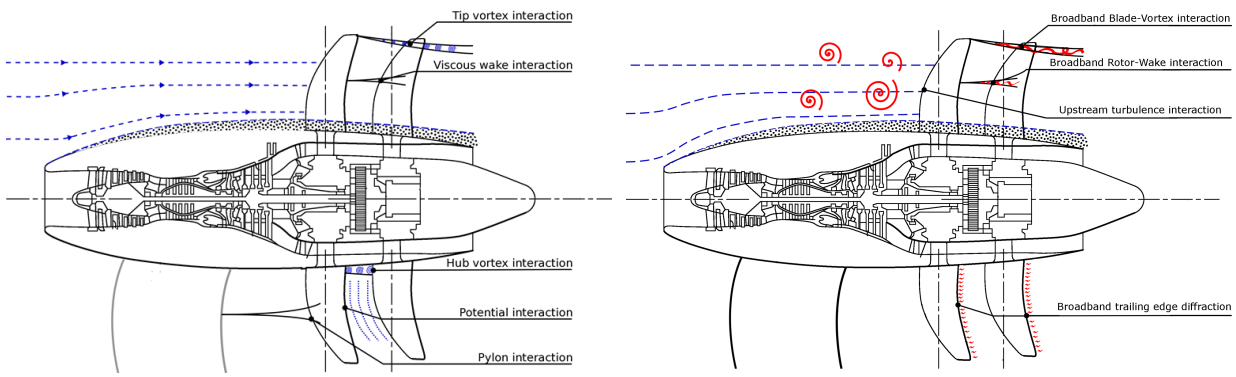

(a) Deterministic velocity fluctuations

(b) Turbulent velocity fluctuations

Figure 1: Velocity fluctuations related to the interaction noise for CROR geometries.

Two noise sources are of interest in this paper: the Orthogonal Blade-Vortex Interaction (OBVI) for the tonal mechanisms and the Broadband Rotor-Wake Interaction (BRWI) for the broadband mechanisms.

A. Tonal noise - OBVI modeling

Tonal noise modeling for CROR is mature for almost every possible fluctuation mechanism. The wake, the potential effect and the pylon interactions were detailed in extensive works performed by Carazo *et al.*,[3] Parry[10] and Jaouani *et al.*[11] respectively and are not going to be investigated in the present work. Concerning the OBVI, previous work was performed in the eighties by Majjigi *et al.*[12] but work is still needed in order to assess the interaction rightfully.[13] It is also of interest to model accurately the OBVI occurring at the tip in order to prepare further investigations on hub-vortex modeling.[14]

The scheme presented in Fig. 2 sums up the basic steps of the tonal model:

1. Based on URANS simulations, the vortex is tracked during its convection in the rotor-rotor volume and the streamline of the vortex core is thus obtained. From a plane normal to the vortex path and close to the leading edge of the aft blades, the maxima of both the tangential and axial velocities are extracted together with the vortex radius. These three parameters are the inputs of an analytical vortex model.

2. Using both the vortex core streamline and the rear rotor geometry, the geometrical features of the OBVI event are computed. For the moment, the vena contracta angle, the helicity of the vortex trajectory and the stagger of the rear blade are used. The upwashes acting on the blade are computed at constant radius and fixed geometrical parameters. These upwashes are expressed into sinusoidal gusts using a double Fourier transform of the periodic impact of vortices on the rear rotor.

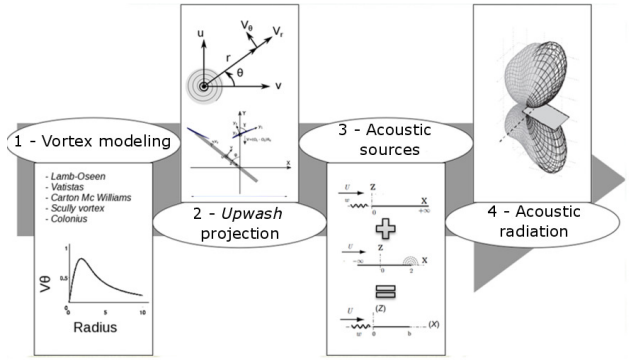

Figure 2: Orthogonal Blade-Vortex Interaction model breakdown

3. Assuming a single flat plate from hub to tip, the unsteady pressure jump is computed using a modified Amiet-Schwarzschild technique taking into account the finite span of the geometry. Two boundary conditions are investigated: one is the classical infinite span methodology, the other is canceling the pressure jump (Kutta condition) at the tip according to previous work performed by Roger *et al.*[15] The local sweep of the blade is taken into account for this part.

4. The unsteady pressure jumps for each loading frequencies radiate in far-field using a frequency-based rotating dipole formulation non-compact both in chord and span.[16] Two geometries are used for the acoustic radiation, a classical Flat Plate (FP) which is representative of the loading part and the Mean Camber Surface (MCS) already used by Carazo[17] for the tonal blade-wake interaction model.

B. Broadband noise - BRWI modeling

Concerning CROR broadband noise, the work performed by Blandeau[18] and Kingan[19] is applied to the same CROR geometry than the OBVI model. The Broadband Rotor Trailing-Edge (BRTE) noise is not considered in this work.

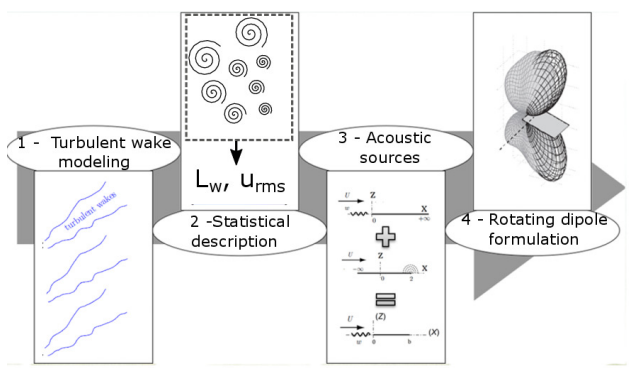

Figure 3: Broadband Rotor-Wake Interaction model breakdown

Figure 3 shows the main steps of the model:

1. From CFD extractions close to the leading edge of the rear rotor, wake turbulent velocities are obtained. Half-wake size (L_w), integral length scale (Λ) and the mean square root of the turbulent velocity (u_{rms}) values are computed.

2. Using the extracted values, assuming a stationary, homogeneous and isotropic turbulence, the turbulent velocity density spectra $\Phi_{ww}^{(2)}$ is computed using 2D empirical models. For this paper, the Von-Karman model is used.[20]

3. The blade loading is then computed using a *strip* theory. The infinite span version of the Amiet-Schwarzschild methodology is used for each strip assuming fixed values of the blade geometry and velocity convection along the strip span.

4. From the blade loading a frequency-based rotating dipole formulation is used in order to compute the far-field noise from the loading acting on the strips. Only the tangential and the axial component of the dipole strength are used for radiation since only the stagger represents the geometry. The far-field noise is computed from flat-plate geometries.

From this methodology, both tonal and broadband noise of a modern CROR geometry can be evaluated. The steps of the methodology constitute the structure of the next section. For each step, the semi-analytical model is going to be benchmarked with numerical results of the same geometry.

III. Results

The geometry used for the comparison is a 12x10 CROR configuration similar to the NASA F31/A31 geometry.[21] The configuration is at approach ($M_X = 0.2$, low rotational speed) and exhibits a strong vena contracta which reactivates the OBVI at the tip of the aft-rotor. The rotational speed $\Omega_1 = \Omega_2 = 86.6$ rad s^{-1}. The distance between the two rotor is approximatively twice the chord and it ensures that the potential interaction noise is low. The aft-rotor is significantly cropped (10 %). The blade geometry is modern, including large chord, sweep, and lean variations along the radius. The numerical setting of an equivalent 12x12 geometry was computed in URANS using *Turb'flow*. The RANS model is a Kok's two equation $k - \omega$ model[22] with a turbulence kinetic energy limiter.[23] The $y+$ is close to 1, ensuring that the boundary layers are correctly modeled. Spatial discretization is second order upwind using AUSM+-up scheme[24] with the Van Albada limiter for conservatives variables. Temporal discretization is a 5-point Runge-Kutta scheme. Acoustic results include numerical FWH results together with a modified Hanson analytical model.[25] First the behavior of the tip-vortex is being investigated and modeled.

A. Tonal noise - OBVI modeling

Before modeling the OBVI event, an introduction to the different Reference Frames (RF) is performed:

RF name	Cartesian coordinates	Cylindrical coordinates	Spherical coordinates
Global RF	(X, Y, Z)	(X, R^c, Φ)	(R^s, Θ^s, Φ)
Unwrapped coordinates RF	$(X, R_{BVI}, R_{BVI}\Phi)$	$\sim$	$\sim$
Vortex local RF	(v_v, u_v, z_v)	(r_v, θ_v, z_v)	$\sim$
Aft-blade surface RF	(x_{c2}, y_{c2}, z_{c2})	$\sim$	$\sim$

Table 1: Description of the reference frames.

Figures 4 show the different frames used in the current approach. The rotational axis of the CROR is X in the global RF. The BVI event occurs at the aft-blade leading edge at the radius R_{BVI} in cylindrical coordinates. At this height the reference frame is locally unwrapped and the blade assumes to move at the constant rectilinear velocity $U_c = R_{BVI}|\Omega_1 - \Omega_2|$ which is the relative velocity seen by an observer attached to the front rotor blades. Typically, vortex models give the behavior of the vortex motion in a cylindrical reference frame attached to the vortex center (r_v, θ_v, z_v) whereas the gust approach requires the velocity fluctuations acting normal to the blade. The RF attached to the aft-blade surface (x_{c2}, y_{c2}, z_{c2}) points to the chordwise, spanwise and normalwise directions respectively.

1. *Vortex modeling*

The first step is to extract the streamline of the vortex core from its inception close to the tip of the front-rotor trailing edge to the leading edge of the aft-rotor. In order to detect the vortex center several research algorithms can be used.[26] In this work, a maximum vorticity method[27] was used in order to extract the streamline from the CFD domain because the vortex is convected outside boundary layers. The extracted

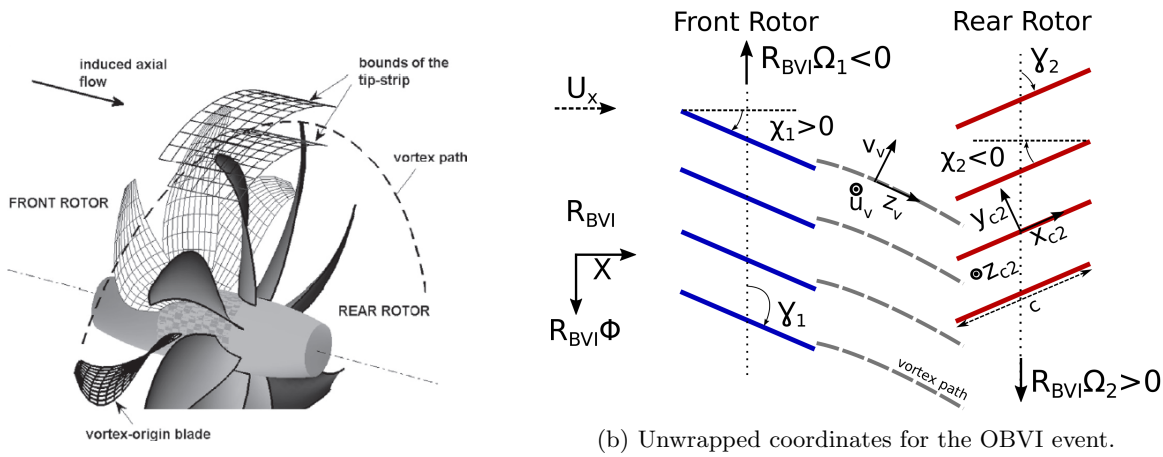

(a) Presentation of the computational case (X, Y, Z).

(b) Unwrapped coordinates for the OBVI event. $(X, R_{BVI}, R_{BVI}\Phi)$.

Figure 4: Presentation of the reference frames, from Roger *et al.*[15]

vortex core streamline was smoothed in order to remove the local instabilities related to its convection and rolling process.[28] A helix equation with a varying radius is used. It reads:

$$\begin{cases} Y_v(X_v) = R_v \cos(b_\varphi X_v + \Phi_{ini}) \\ Z_v(X_v) = R_v \sin(b_\varphi X_v + \Phi_{ini}) \end{cases}, \tag{2}$$

where (X_v, Y_v, Z_v) are the vortex core streamline trajectory in Cartesian coordinates (X, Y, Z), R_v is the radius in the cylindrical coordinates, b_φ is the lead and Φ_{ini} is the angular origin of the helix. Because of the vena contracta, the R_v is modified along X_v. In order to model this variation, a linear variation of the vortex-core radius is used:

$$R_v(X_v) = \alpha_\beta X_v + R_{ini}, \tag{3}$$

with α_β the coefficient related to the vena contracta angle and R_{ini} related to the initial radius of the helix. The linear regression was used over classical linear-rational formulation[12] because of CFD extractions and recent experimental extractions on the F31/A31 geometry.[21] The smoothed streamline is used in order to simplify the extraction of the OBVI geometrical parameters. Figure 5a shows the trajectory. It compares the quality of the smoothed streamline with direct CFD extractions. Small differences can be seen on the trajectory thus the regression captures the behavior of the vortex core accurately.

From Figure 5b the smoothed streamline (the blue points) is used to extract the relative vortex velocities in the local vortex reference frame (r_v, θ_v, z_v) using a disc locally normal to the trajectory and making the vortex center the local origin of the reference frame. Because the vortex is not purely axisymmetric the results on the disc are interpolated on a local grid uniform in azimuth. From this grid, the azimuthal mean is computed for both the azimuthal and axial local velocities. Figure 6 shows the result of the extractions for three different axial positions: one close to the front rotor trailing edge, one approximatively at half distance between the front and aft rotors and one extracted as close as possible from the BVI event. Figures 6a and 6b show that the vortex dissipates during its convection from the front to the rear rotor. The pressure deficit behavior (Fig. 6c) is related to a local radial equilibrium that can be seen in several other vortex extractions.[29]

From the latest plane (85 % $R_1 - R_2$ distance), the maximum azimuthal V_θ^{max} and axial V_x^{max} velocities are extracted together with the vortex core radius r_0 in the vortex RF (r_v, θ_v, z_v). V_θ^{max} and r_0 are used in order to feed tangential velocity models such as Lamb-Oseen, Scully or Taylor vortices[29] whose formulas are:

$$V_\theta^{LO}(r) = \frac{V_\theta^{max} r_0}{r} \frac{1 - e^{-\alpha^2 (r/r_0)^2}}{1 - e^{-\alpha^2}}, \quad V_\theta^{Sc}(r) = \frac{2 V_\theta^{max} r}{r_0 \left((r/r_0)^2 + 1\right)}, \quad V_\theta^{Ta}(r) = \frac{V_\theta^{max} r}{r_0} e^{\frac{1}{2}\left(1 - (r/r_0)^2\right)}, \tag{4}$$

where the coefficient $\alpha \approx 1.121$ is made in order to have the peak velocity at $r = r_0$ for the Lamb-Oseen vortex. Figure 7a shows the behavior of the Lamb-Oseen model compared with CFD extractions.

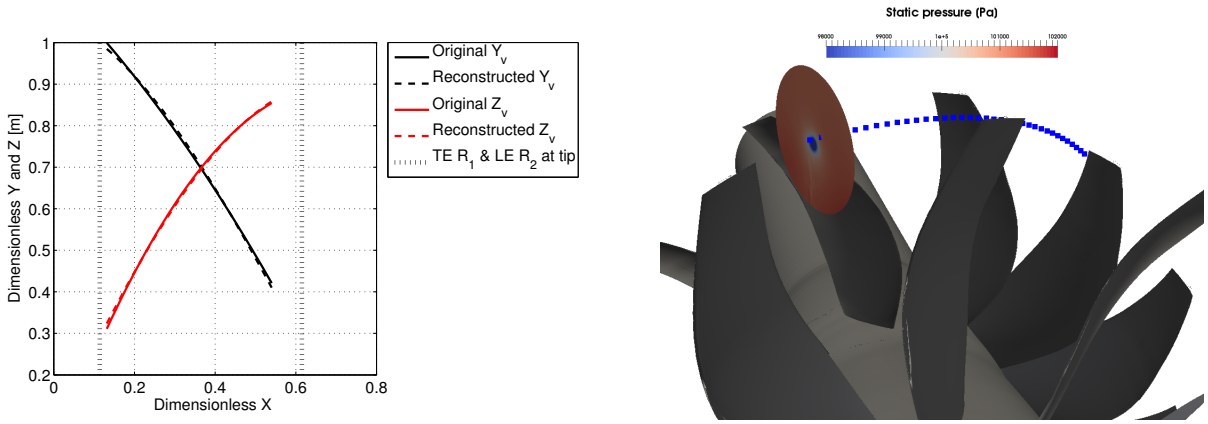

(a) Extracted and reconstructed trajectories.

(b) Global view of the extraction procedure.

Figure 5: The vortex extraction procedure, using the current CROR geometry presented by Soulat *et al.*,[25] trajectories are made dimensionless by the front rotor tip radius.

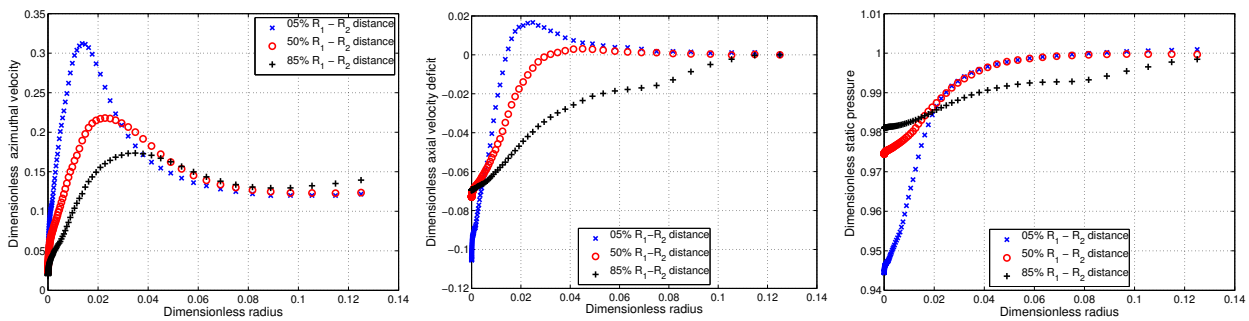

(a) Tangential velocity.

(b) Axial velocity.

(c) Static pressure.

Figure 6: Vortex extractions for different axial positions. Velocities, distances and pressure are respectively made dimensionless by the front rotor tip velocity, the front rotor radius and the atmospheric pressure.

Discrepancies between the results are attributed to the convection velocity that is not purely normal to the extraction plane. The axial velocity was also considered since it was shown as fundamental in OBVI noise for CROR.[30] A classical Gaussian velocity deficit formulation can be used:[28]

$$V_x^{Gau}(r) = V_x^{max} \exp\left(-\left[r/r_0\right]^2\right). \tag{5}$$

Figure 7b shows that the Gaussian velocity fairly predicts the axial behavior of the vortex.

In order to check the quality of the analytical model and confirm that the discrepancies between the extractions and the analytical model in Fig. 7a comes from the convection velocity of the vortex, a recomposition of the radial velocity fluctuations was produced by the analytical velocity and compared with CFD extractions. Figures 8a and 8b show that the analytical model captures fairly well the velocity fluctuations in the global reference frame. Note that only the tangential velocity was used for the recomposition of the radial velocity.

For the sake of brevity, results for the analytical models are only showed for the Lamb-Oseen model coupled with the axial velocity deficit using a Gaussian formulation. From these vortex velocity extractions and assuming the classical gust procedure, let's compute the upwash acting on the blade.

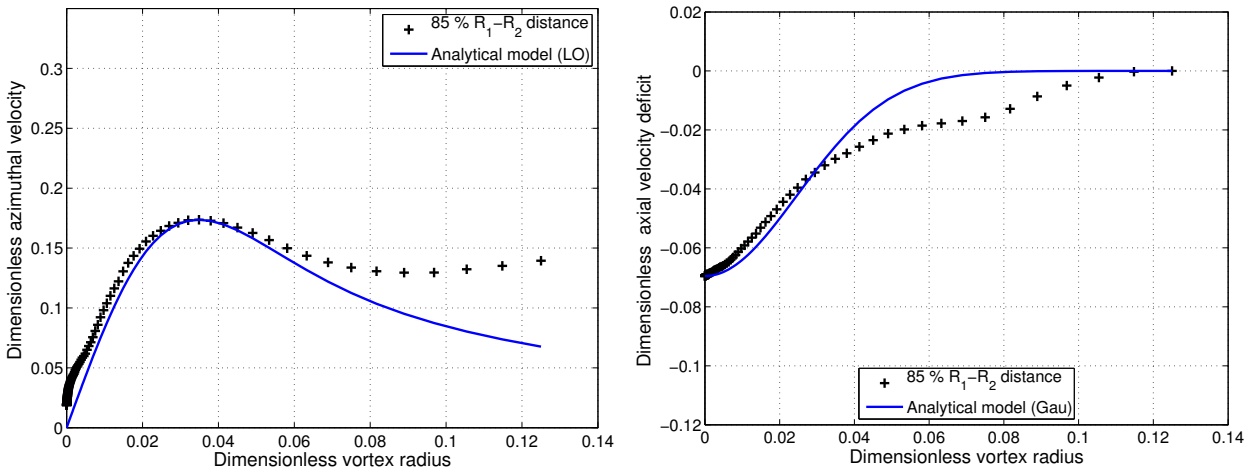

(a) Tangential velocity.

(b) Axial velocity.

Figure 7: Numerical and analytical tangential and axial velocity comparison for the 85% extraction plane, in the vortex reference frame (r_v, θ_v, z_v).

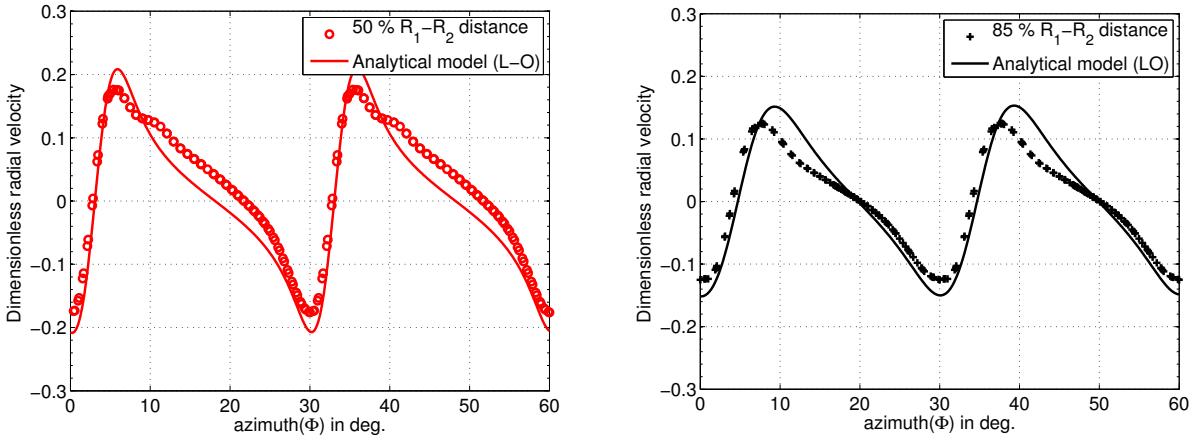

(a) 50% tip $R_1 - R_2$ distance.

(b) 85% tip $R_1 - R_2$ distance.

Figure 8: Radial velocity comparison between numerical extractions and the analytical model using the global reference frame (X, Y, Z).

2. *Upwash computation*

Figure 4a shows that the vortex shed by the front meshed blade is convected to the aft blade tip region within the bounds of the tip-strip. Between the bounds of the tip-strip the convection velocity of the vortex is assumed constant. This means that the radius of the vortex r_0 is significantly smaller than the radius at which the BVI event occurs R_{BVI} (i.e $R_{BVI} >> r_0$). The upwashes are the velocity fluctuations in the y_{c2} direction for $y_{c2} = 0$. The aft blade stagger angle is noted γ_2 and the angle made between the front blade tip-vortex path and the rear blade displacement direction is named φ. The vena contracta angle β is introduced in an intermediate reference frame between the (r_v, θ_v, z_v) and the locally unwrapped direct $(X, R_{BVI}, R_{BVI}\Phi)$ reference frame. $a_\beta x$ is related to the vena contracta angle and b_φ is related to the

helicity of the vortex using the formulas:

$$\begin{cases} \beta = \text{atan}(a_\beta) \\ \varphi = \text{atan}(\dfrac{1}{b_\varphi R_{BVI}}) \end{cases} \tag{6}$$

These parameters allow to project the vortex velocities in the blade reference frame according to:

$$\text{w}(x_{c2}, 0, z_{c2}, t) = (V_x(r)\hat{e}_{z_v} + V_\theta(r)\hat{e}_{\theta_v}).\hat{e}_{y_{c2}}, \tag{7}$$

with $\hat{e}_{\theta_v}$ and $\hat{e}_{z_v}$ the basis vectors of the (r_v, θ_v, z_v) reference frame. This upwash is turned into sinusoidal gusts using a double spatial Fourier transform along the local chordwise (k_x) and spanwise (k_z) directions. It reads:

$$G(k_x, k_z) = \frac{1}{(2\pi)^2} \int_{-\infty}^{+\infty} \int_{-\infty}^{+\infty} \tilde{\text{w}}(x_{c2}, 0, z_{c2}, \omega_s) e^{-i(k_x x_{c2} + k_z z_{c2})} dx_{c2} dz_{c2}, \tag{8}$$

where $\tilde{\text{w}}$ is the temporal Fourier transform of upwash assuming $\exp(-i\omega_s t)$ is the Fourier transform convention for monochromatic waves and positive frequencies. From Quaglia *et al.*,[1] the 2D upwash density spectra from all the aforementioned vortex models including vena contracta effects are computed. Looking only the Lamb-Oseen formula, it reads:

$$G^{LO}(k_x, k_z) = \frac{iC_{amp}^{LO}}{2\pi U_c \sin(\varphi + \gamma_2)} \left[\frac{C_{span} k_z}{c_\beta} - \frac{C_{chord} 2abk_x}{\sin(\varphi + \gamma_2)} \right] \frac{e^{-a^2 k_x^2 - \frac{k_z^2}{4b^2}}}{(2abk_x)^2 + k_z^2}, \tag{9}$$

where C_{amp}^{LO} is equal to $V_\theta^{max} r_0/[1 - \exp(-\alpha^2)]$, $a = r_0/(2\sqrt{\alpha}\sin(\varphi + \gamma_2))$, $b = \alpha c_\beta / r_0$ are related to the chordwise and spanwise developments of the Lamb-Oseen vortex and $c_\beta = (1 - \tan^2\beta)^{0.5}$. Similar developments leads to the upwash spectral distribution of the axial velocity:

$$G^{Gau}(k_x, k_z) = \frac{-V_x^{max}\cos(\beta) r_0}{4\pi U_c c_\beta} \exp\left[-\left(\frac{k_x r_0}{2\sin(\varphi + \gamma)} \right)^2 - \left(\frac{k_z r_0}{2c_\beta} \right)^2 \right]. \tag{10}$$

Figure 9a shows the upwash density map for a Lamb-Oseen vortex coupled with an Gaussian axial velocity deficit configured using the streamline and blade from Fig. 5b. Because the velocity fluctuations coming from the tangential and axial contributions are orthogonal, the sum of the two upwash spectral distributions gives the total upwash for the 3D model:

$$G(k_x, k_y z) = G^{Gau}(k_x, k_z) + G^{LO}(k_x, k_z). \tag{11}$$

The adjacent front-rotor blade will shed a similar vortex which is going to impinge the same aft blade at $t_{adj} = t + \Delta t$. $\Delta t = 2\pi/(B_1|\Omega_1 - \Omega_2|)$ is the delay between two consecutive BVI events. For the CROR case, it reads:

$$f_\text{w} = \sum_{m=-\infty}^{+\infty} \text{w}(x_{c2}, 0, z_{c2}, t - m\Delta t) = \text{w}(x_{c2}, 0, z_{c2}, t) \star \sum_{m=-\infty}^{+\infty} \delta(t - m\Delta t). \tag{12}$$

The Fourier series of the above train of vortices gives:

$$\tilde{f}_\text{w} = \sum_{m=-\infty}^{+\infty} \frac{2\pi}{\Delta t} \tilde{\text{w}}\left(x_{c2}, 0, z_{c2}, \omega_s\right) \delta(\omega_s - m2\pi/\Delta t). \tag{13}$$

So for each harmonic loading :

$$\omega_m = mB_1|\Omega_1 - \Omega_2|, \tag{14}$$

only a constant k_x slice of the map is extracted for $k_{x,m} = \omega_m / U_c$. Figure 9 gives the upwash distributions used in order to compute the noise for the first three harmonics. The effect of the vena contracta moves the maxima of the peaks along the k_z axis for increasing values of k_x.

The impingement of upwashes at the leading edge of the aft-rotor blades will create an unsteady loading on the blades. Using sinusoidal upwashes, the Amiet-Schwarzschild theory[31] is used in order to compute the unsteady loading acting on the aft-rotor blades.

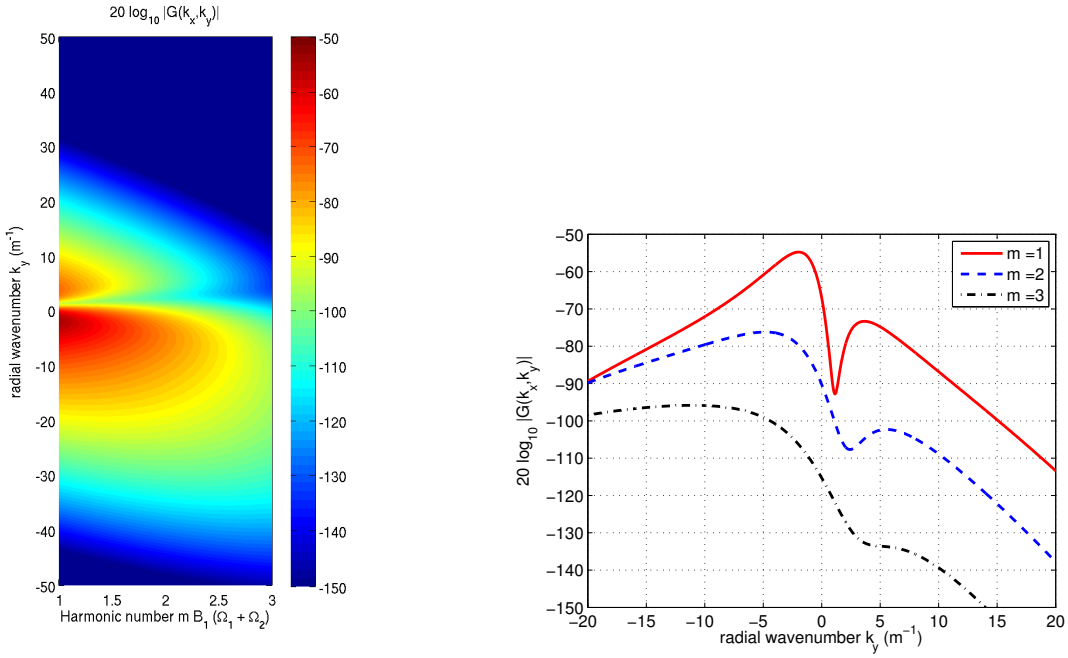

(a) Spectral upwash distribution.

(b) Extraction for several harmonics.

Figure 9: Upwash density for a Lamb-Oseen vortex + Gaussian axial velocity, configured using the streamline presented in Fig. 5.

3. *Blade loading*

Having described the upwash excitation, the blade response can then be computed for each incoming gust. The unsteady aerodynamics are derived from Amiet-Schwarzschild theory,[31] adapted for the case of infinitely thin, swept, finite chord (c), infinite span airfoils using the linearized flow theory.[32,15,33] A sinusoidal upwash described by $\mathrm{w}(x'_{c2}, z'_{c2}, t) = \tilde{\mathrm{w}}(k_x, k_z)\exp(i(k'_x x'_{c2} + k'_z z'_{c2} - \omega_s t))$ is convected over the airfoil at the oblique speed:

$$U_c \hat{e}_{z_1} = |\Omega_2| R_{BVI} \cos\beta \vec{e}_{x_{c2}} - |\Omega_2| R_{BVI} \sin\beta \vec{e}_{z_{c2}} = U_1 \vec{e}_{x_{c2}} + U_2 \vec{e}_{z_{c2}}. \tag{15}$$

Note, that U_c is now defined according to the local rotational speed of the aft-blade whereas it was defined according to the gust convection velocity in the previous part. Like Roger and Moreau,[34] a free-stream to convection speed ratio could be used but is not implemented yet. The reference frame $(x'_{c2}, y_{c2}, z'_{c2})$ is related to the swept blade reference frame presented in Fig. 10. The link between the wavenumbers is:

$$k_x = \cos\Psi k'_x + \sin\Psi k'_z, \quad k_z = -\sin\Psi k'_x + \cos\Psi k'_z. \tag{16}$$

The impingement of the gust generates a potential velocity disturbance $\vec{u}' = \nabla\Phi'$ (considering an irrotational velocity disturbance) such that Φ' is the solution of the canonical, dimensionless Helmholtz equation:

$$\frac{\partial^2\Phi'}{\partial^2 x'^*_{c2}} + \frac{\partial^2\Phi'}{\partial^2 y^*_{c2}} + \kappa^2\Phi' = 0, \tag{17}$$

where $\kappa^2 = (\mu^2 - k'^*_z/\beta_1^2)$ is the dimensionless Helmholtz, $\mu = k'^*_x M_1/\beta_1^2$. $\beta_1 = \sqrt{1-M_1^2}$ and $\beta_2 = \sqrt{1-M_2^2}$ are the chordwise and spanwise compressibility coefficients respectively, M_1 and M_2 being the corresponding Mach numbers. The superscript $*$ means that distances and wavenumbers are made dimensionless by the half-chord ($c/2$).

The boundary conditions on the blade ($y_{c2} = 0$) of the problem are:

- Zero potential upstream of the leading-edge: $\Phi' = 0$, $x'^*_{c2} < 0$.
- Zero normal velocity on the airfoil surface: $\partial\Phi'(x'^*_{c2}, 0, z'^*_{c2})/(\partial y_{c2}) = 0$, $0 < x'^*_{c2} < 2$.

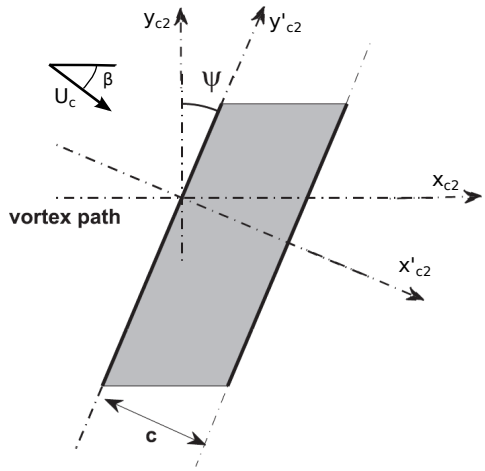

Figure 10: Schematic of the swept moving blade reference frame, from Roger *et al.*[15] Note that for realistic CROR geometries, β is inferior to the local sweep Ψ.

- Zero pressure jump at the trailing-edge (Kutta condition): $\tilde{p}'(x'^*_{c2}, 0, z'^*_{c2}) = 0$, $x'^*_{c2} > 2$.

From this set of equations, for high frequencies relative to the chord of the blade, a two-steps solution is obtained. The first step meets the boundary conditions at the leading edge (cancellation of the incoming upwash) and assumes an infinite chord problem downstream of the leading edge. The second solution corrects the first one assuming a Kutta condition at the trailing edge. The solutions for the first (Φ'_{LE}) and second (Φ'_{TE}) iterations yield the corresponding surface pressure using the momentum conservation equations[31] expressed as:

$$\begin{aligned}
&\tilde{p}_{LE}(x'^*_{c2}, 0, z'^*_{c2}, k^*_x, k^*_z) = -\rho_0 U_1 \tilde{\mathrm{w}} \frac{\exp(-i(\mu M_1 - \kappa)x'^*_{c2} + ik'^*_z z'^*_{c2} + i\pi/4)\exp(-i\omega_s t)}{\sqrt{\pi(k'^*_x + \beta_1^2\kappa)x'^*_{c2}}}, \\
&\tilde{p}_{TE}(x'^*_{c2}, 0, z'^*_{c2}, k^*_x, k^*_z) = \rho_0 U_1 \tilde{\mathrm{w}} \\
&\times \frac{\exp(-i(\mu M_1 - \kappa)x'^*_{c2} + ik'^*_z z'^*_{c2} + i\pi/4)\exp(-i\omega_s t)}{\sqrt{\pi(k'^*_x + \beta_1^2\kappa)}} \left[1 - (1+i)E^*(2\mu(2 - x'^*_{c2}))\right].
\end{aligned} \tag{18}$$

The corresponding lift or pressure jump $\tilde{l}_{LE}$ and $\tilde{l}_{TE}$ is twice the disturbance pressure since the pressure fluctuations ($\tilde{p}'$) have opposite phases on both sides. E^* is the complex conjugate of the Fresnel integral as defined by Amiet.[31] The aforementioned formulas are valid for supercritical gusts. For subcritical gusts, a modified value of $i\kappa' = i\sqrt{-\kappa^2}$ is used, the term involving E^* becomes $1 - \mathrm{erf}([2\kappa'(2 - x'^*_{c2})]^{0.5})$. The total pressure jump is sum of the leading edge and trailing edge contribution $\tilde{l}_{TOT} = \tilde{l}_{LE} + \tilde{l}_{TE}$.

These formula are given for a fixed value of the span wavenumber k'_y and were validated using the results from Roger *et al.*[15] . In order to recompose the total pressure jumps acting on the flat plate for one harmonic loading pulsation ω_m, an infinite summation of all the skewed gust is performed. The total m^{th} harmonic pressure jump is thus:

$$\Delta\tilde{p}_m(x'^*_{c2}, 0, z'^*_{c2}) = \int_{-\infty}^{+\infty} \tilde{l}_{TOT}(x'^*_{c2}, 0, z'^*_{c2}, k^*_{x,m}, k^*_z) dk^*_z, \tag{19}$$

where $k^*_{x,m} = k_{x,m}c/2$ is the dimensionless wavenumber of the mth harmonic loading. Figures 11 compare the analytical and the numerical pressure jumps acting on the blade for different harmonics. Only a single flat plate was used in order to compute the results. This flat plate extends from hub to tip because for low interaction frequencies large equivalent wavenumbers can be seen on the blade.[35] These dimensionless maps are 2D structured grid used in order to compute the local dipole forces for the acoustic radiation. Using this description, the position of one local dipole is described using a pair of indexes (i, j) representing the chordwise and spanwise directions respectively.

Looking at the analytical blade responses, the assumption of infinite span can be criticized. Indeed the response seems to be sharply cut at the tip but apparently the major difference between the analytical

and the numerical results is a strong patch of unsteady lift located at 80% of the chord and at 98% of the span. This difference may come from two physical mechanisms. First, for CROR swept blades, leading edge vortices[36] can be seen grazing the surface from mid-span to tip. This leading edge vortex may modify the pressure jump because it dynamically interacts with the incoming velocities.[37] The second physical mechanism is the fact that the edge of the blade can be considered as a leading edge because of the vena contracta. Despite these differences it appears that the infinite span model correctly predict the decreasing intensity of the vortex impact for all frequencies at the leading edge. For low frequency one can see that the equivalent wavelengths of the vortex impact are so large that it is not possible to truncate the flat plate in the radial direction.

These dimensionless maps of pressure jump are the acoustic sources of the rotating dipole acoustic analogy which is thereafter presented.

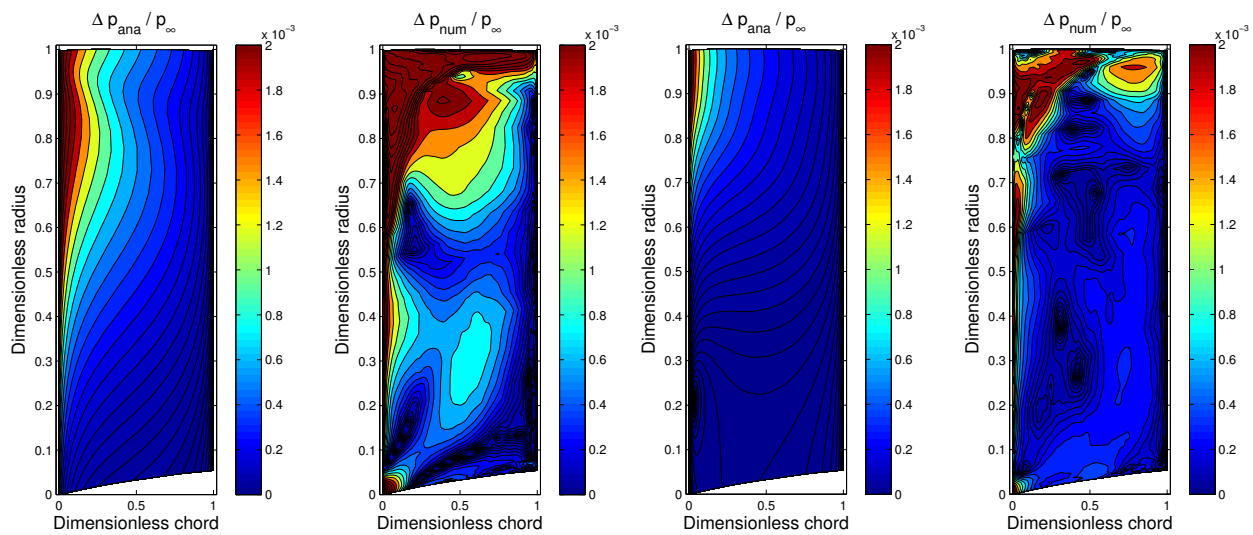

(a) Comparison for 1st Harmonic ($m = 1$) (b) Comparison for 2nd Harmonic ($m = 2$)

Figure 11: Dimensionless contours of the pressure jump computed using the Amiet-Schwarzschild method and extracted from CFD for different loading harmonics. $p_\infty = p_{atm}$. 50 logarithmic contours.

4. *Acoustic radiation*

Now that the pressure jumps are evaluated, the acoustic results are obtained using a frequency-based rotating dipole formulation of the FWH equation for CROR. The far-field non-compact both in chord and span formula from Hanson and Parzych[16] is used here. Only the loading term of the formulation is kept here. The acoustic pressure for an observer $\vec{X}_o = (R_o, \Theta_o, \Phi_o)$ in the spherical global reference frame received from one acoustic source lattice (i, j) located at $\vec{y} = (X_s, R_s, \Phi_s)$ described in cylindrical coordinates reads:

$$\begin{aligned} p_{ac}(\vec{X}, t) = & \frac{-iB_2}{4\pi S_0} \sum_m \sum_n k_{m,n} e^{ik_{m,n}\left(R_o - \frac{cos(\Theta_e)}{D_c}[X_o - X_s] - t\right)} e^{i[(mB_1 - nB_2)(\Phi_o - \pi/2 - \Phi_s)]} \\ & \times \left\{ iS_s \tilde{F}_m^R(i,j) J'_{mB_1 - nB_2}(k_{m,n} S_s R_s) + \frac{mB_1 - nB_2}{k_{m,n} R_o} \tilde{F}_m^\Phi(i,j) J_{mB_1 - nB_2}(k_{m,n} S_s R_s) \right. \\ & \left. + S_c \tilde{F}_m^X(i,j) J_{mB_1 - nB_2}(k_{m,n} S_s R_s) \right\}. \end{aligned} \tag{20}$$

S_0 is the far-field source-observer distance, S_c and S_s are the cosine and sinus of the polar angle corrected by the convection velocity ($U_X = M_X c_0$) in the global reference frame respectively defined by Hanson and Parzych.[16] The subscript e is related to emission coordinates. X_o is the axial distance of the observer in the cylindrical coordinates and $J_\nu(x)$ are the Bessel functions of first kind. The dipole vector $\tilde{F}_m(i,j) = (\tilde{F}_m^X(i,j), \tilde{F}_m^R(i,j), \tilde{F}_m^\Phi(i,j))$ are the local components of a single panel at the harmonic loading m described in Eq. (14) and associated with one acoustic interaction wavenumber $k_{m,n} = (mB_1\Omega_1 + nB_2\Omega_2)/c_0$ in

the axial, radial and azimuthal direction respectively. $|\tilde{F}_m(i,j)|$ is obtained by a numerical quadrature of pressure jumps of the Eq. (19):

$$|\tilde{F}_{m,n}(i,j)| = \frac{S_{i,j}}{4}\left(\Delta\tilde{p}_m(i-1/2,j-1/2) + \Delta\tilde{p}_m(i+1/2,j-1/2)\right.$$
$$\left.+\Delta\tilde{p}_m(i-1/2,j+1/2) + \Delta\tilde{p}_m(i+1/2,j+1/2)\right), \tag{21}$$

$S_{i,j}$ is the surface of the local lattice. The normal (pointing from suction side to the pressure side) is computed using the cross product of the local vector of the lattice (i,j).

The results presented in this part are threefold. First a full numerical temporal formulation of the FWH is the baseline of our modeling. It uses the acoustic sources coming from the CFD. The FWH formulation is advancing in time and computes both the thickness and the loading terms of the FWH equation. However, preliminary investigations showed that the thickness noise is negligible compared with the loading for the first interaction tone ($BPF_1 + BPF_2$) because of the approach condition and the low rotational speed. For the loading noise, the numerically solved equation comes from Casalino.[38] The second case uses the sources from the CFD but the frequency-domain rotating dipole formulation given by Eq. (20) is used for the acoustic propagation. This second case was made in order to validate the rotating dipole formulation. To finish, the semi-analytical OBVI model is going to be used and compared with other results.

The microphones are sideline and located 20 meters away from the geometry rotational axis as presented in Fig. 12a. The axial zero position for the computation of the polar angles is located between the two rotors. The flow axis is pointing downstream and the polar origin ($\Theta^s = 0$) coincides with the flow axis.

Figure 12b presents the MCS of the current blade geometry. This geometry is obtained by extruding the mean camber lines of the profile taken at different radial location. The flat plate extends from hub to tip and only takes into account the stagger γ_2 of the aft-rotor blade at the BVI event radius.

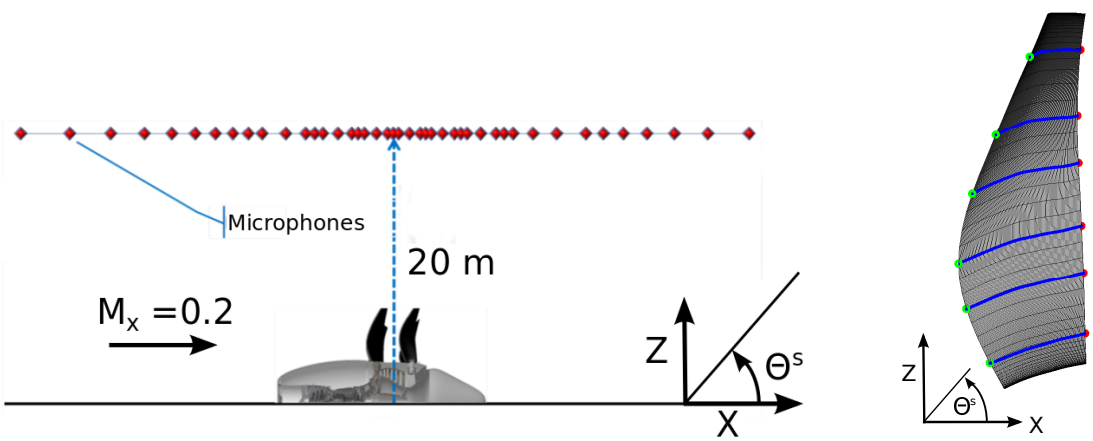

(a) Position of the far-field microphones.

(b) MCS of the rear blade.

Figure 12: Microphones positions for the BRWI test case and blade surface (MCS) for the acoustic radiation. Green circles are the leading edges, red circles are the trailing edges, blue lines are the profiles on the surface mesh and the black surface is the MCS.

Figure 13 shows the acoustic pressure obtained for every model and interaction tones. For the first interaction tone ($BPF_1 + BPF_2$), the analytical model fairly captures the directivity in the backward arc ($0 \rightarrow 90°$), the lobes are correctly predicted and a 3 dB difference exists between the analytical model and the numerical results. On the contrary, the forward arc neither gets the lobes nor levels when compared with numerical results. A 10 dB difference can be seen at the 110° lobe. This is attributed to a misprediction of the loading at the tip. For higher harmonics, the analytical model fairly recovers the numerical results. The use of the MCS when compared with the flat plate is justified because it gets the good directivity of the local dipoles. This can be seen especially around the rotational plane.

To conclude, the current OBVI model gives acceptable results compared with numerical FWH solutions when using the MCS geometry. The results are especially good in the rotational plane and in the backward

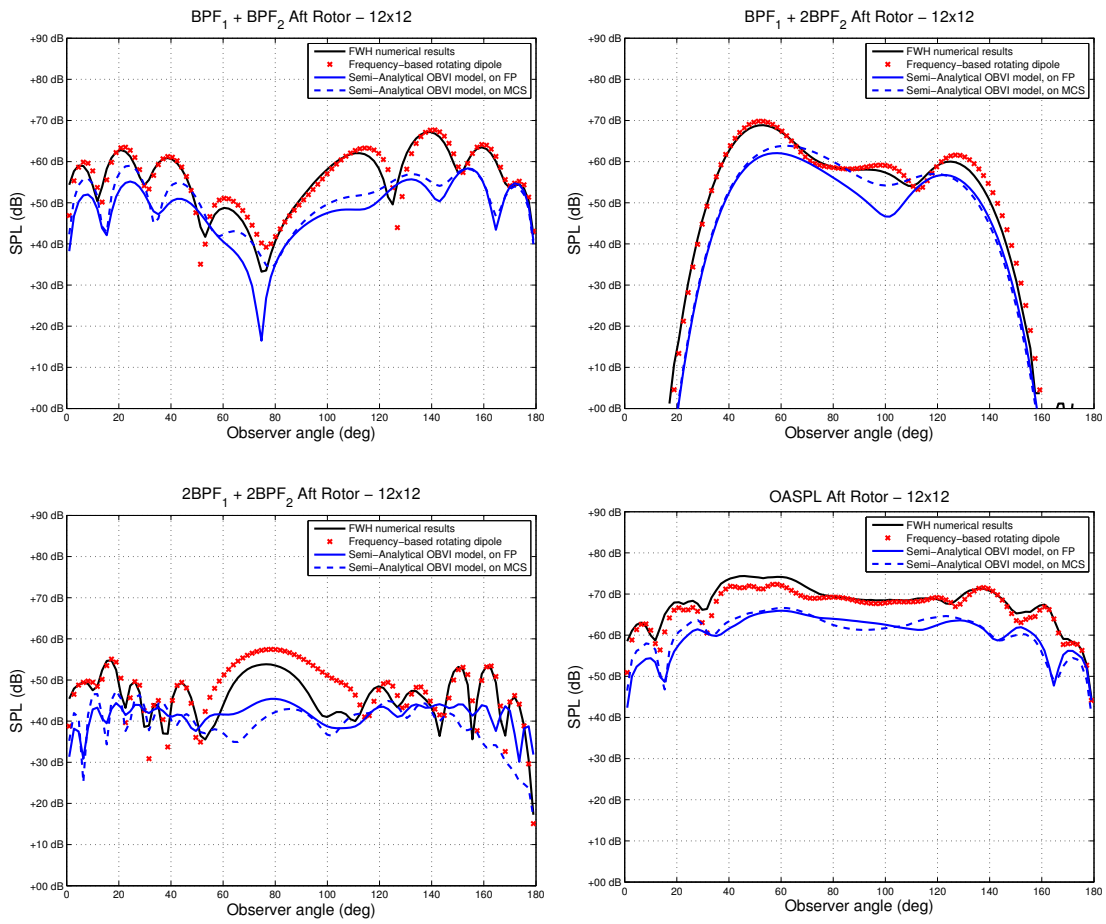

Figure 13: Sound Pressure Levels (SPL) comparison for different harmonic frequencies for the aft rotor. FWH are full numerical results, H-P are rotating dipole results using the frequency approach for far-field radiation and FP uses a flat plate for the acoustic radiation.

arc for all frequencies. Large discrepancies can still be seen in the forward arc and for high frequencies. These differences are attributed to the discrepancies in the loading part where the infinite span assumption no longer represents the physics at the tip. A first modification for the loading part could take into account the tip using a modified Amiet-Schwarzschild theory described by Roger *et al.*[15] It assumes that the tip is a trailing edge and uses a Kutta condition at the edge of the blade.

B. Broadband noise - BRWI modeling

1. Description of the model

The BRWI model derived from Blandeau *et al.*[2] is for a single strip, located at a radius R_s with a ΔR span:

$$S_{pp}(\vec{X},\omega_s) = \frac{B_2}{(4\pi)R_o^2\sqrt{1-M_X^2\sin\Theta_o}^2}\sum_{m=-\infty}^{+\infty}\sum_{n=-\infty}^{+\infty} \int_{R_s-\Delta R/2}^{R_s+\Delta R/2} \pi U_1 D_{m,n}(R)^2 \Phi_{ww}^{(2)}(k_{x,mn},0)\left|\mathcal{L}_{m,n}(k_{x,n},\kappa_n,\omega_s)\right|^2 dR, \tag{22}$$

using again $\vec{X} = (X_o, R_o, \Theta_o)$ as observer coordinates and with:

$$D_{m,n}(R) = f_m(R,\chi_1)\left[\frac{k_s\cos\Theta_o\sin(\chi_2)}{\beta_X^2\sqrt{1-M_X^2\sin^2\Theta_o}} + \frac{l\cos(\chi_2)}{R}\right] J_l\left(\frac{k_s R\sin\Theta_o}{\sqrt{1-M_x^2\sin^2\Theta_o}}\right) \tag{23}$$

with $k_s = \omega_s/c_0$ the acoustic wavenumber and $\chi_* = \pi/2 - \gamma_*$ the stagger of the blades defined this time from the rotational axis with the subscript $*$ taking the values 1 or 2 for the front and aft blade respectively. The aerodynamic-aeroacoustic wavenumber κ_n reads:

$$\kappa_n(R) = \frac{n\sin(\chi_2)}{R} - \frac{k_s\cos(\chi_2)}{\beta_X^2}\left(\frac{\cos\Theta_o}{\sqrt{1-M_X^2\sin^2\Theta_o}} - M_X\right). \tag{24}$$

The wavenumbers in the chordwise direction of the aft-rotor blades for incoming turbulent velocity $k_{x,mn}$ and the frequency-based rotating dipole formulation $k_{x,n}$ are defined by:

$$\begin{cases} k_{x,mn} = \dfrac{\omega_s - n\Omega_2 - mB_1|\Omega_1-\Omega_2|}{U_1} \\ k_{x,n} = \dfrac{\omega_s - n|\Omega_2|}{U_1} \end{cases}. \tag{25}$$

The $\mathcal{L}_{m,n}(k_{x,n},\kappa_n,\omega_s)$ function is the radiation integral for rotating flat plate. It uses both the isolated blade response for turbulence interaction with trailing-edge backscattering[39] and a low-frequency incompressible formulation.[40] The only geometrical parameters for the radiating geometry is the aft-blade stagger. Only gusts parallel to the leading edge are considered.

$f_m(R,\chi_1)$ is the dimensionless modulation function used in order to modulate the incoming turbulent velocity seen in the wakes. This is based on the work by Ventres *et al.*[41] and was used for turbofans BRWI noise model.[42] It is based on the fact that the wakes are symmetric Gaussian functions with a single parameter, the half-wake size. It reads:

$$f_m(R,\chi_1) = \frac{1}{B_1\sigma(R,\chi_1)\sqrt{2\pi}}\exp\left\{-\frac{1}{2}\left(\frac{m}{\sigma(R,\chi_1)}\right)^2\right\}, \tag{26}$$

with:

$$\sigma(R,\chi_1) = \frac{R\cos(\chi_1)\sqrt{2\ln(2)}}{B_1 L_w}. \tag{27}$$

The turbulence modeling used in our case uses an isotropic, homogeneous 2D Von Karman spectrum defined by:

$$\Phi_{\mathrm{ww}}^{(2)}(k_x,k_y) = \frac{4}{9\pi}\frac{u_{rms}^2}{k_e^4}\frac{k_x^2+k_y^2}{\left(1+(k_x^2+k_y^2)/k_e^2\right)^{7/3}}, \tag{28}$$

where $k_e = \Gamma(5/6)/\Gamma(1/3)\cdot\sqrt{\pi}/\Lambda$ is the wavenumber associated with the turbulence, similar to the OBVI model (k_x, k_y) are the wavenumbers respectively in the chordwise and spanwise directions. Γ is the upper incomplete Gamma function.

2. *Validation of the model implementation*

The implementation of the model is first being validated using the canonical definition given by Blandeau *et al.*[2] Figure 14a introduces the geometry. It consists in a single strip located at $r_s = 1$ m, of span $\Delta r = 0.2$ m. The chord is 0.3 m. The front and rear number of blades are 10 and 5 respectively. The stagger angles are similar between the front and rear blades $\gamma_1 = \gamma_2 = \pi/4$. The rotor speed is $\Omega_1 = \Omega_2 = 170$ rad s^{-1}. The convection speed is $U_1 = 240$ m s^{-1}. The turbulent wake parameters are $\Lambda = 0.04$ m, $u_{rms} = 4.8$ m s^{-1} and the half-wake $L_w = 0.095$ m. $\rho_0 = 1.2$ kg m^{-3} and $c_0 = 340$ m s^{-1}. Figure 14b shows the results of the Sound power level (PWL) of the current model compared with the results by Blandeau *et al.*[2] It appears that less than 0.5 dB is found between the two implementations for all frequencies. This validates the implemented model and the BRWI model can be used on the same geometry than the OBVI model.

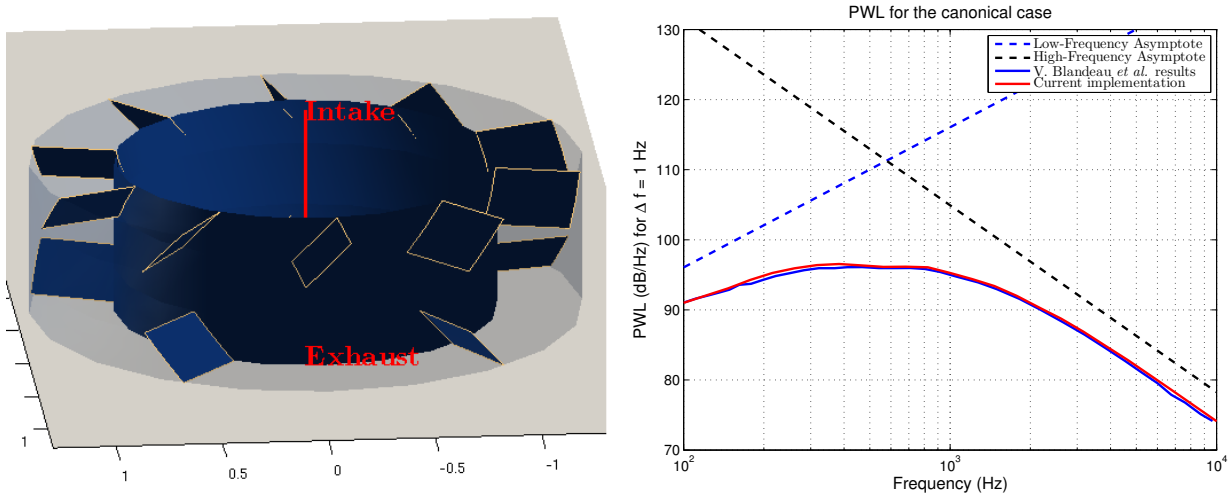

(a) Canonical geometry

(b) Power spectra results for both implementations.

Figure 14: Canonical validation used for the BRWI code, presented by Blandeau *et al.*[2]

3. *Application to the current geometry*

First, significant aerodynamic variables coming from CFD are extracted close to the leading edge of the rear rotor following the procedure described by Carazo.[17] A temporal mean of the aerodynamic variables is performed in the reference frame rotating with the front-rotor blades. Figure 15a shows the axial velocity fluctuation maps used in order to extract the half-wake size. In this map, the azimuthal mean of the axial velocity is removed for each radius in order to clearly see the wakes. Figures 15b and 15c show the extractions of the turbulent quantities from CFD. It appears that once again the front-rotor tip vortex plays an important role in the broadband noise since the maximum of turbulent kinetic energy (k) can be found in the vortex region. The map of specific dissipation shows very well the wakes coming from the front rotor, however once again, the interaction seems to largely be tip-driven.

Extractions of Λ, u_{rms} and L_{w} were made for each radius. Figure 16a shows the behavior of Λ along the radius reconstructed using both the turbulent variables using:

$$\Lambda = \frac{k^{1.5}}{\varepsilon}, \tag{29}$$

with $\varepsilon = \rho C_\nu k \omega$ the turbulent dissipation from $k - \varepsilon$ RANS models.[43] ρ is the fluid density and $C_\nu = 0.09$. Another far-wake model described by Jurdic *et al.*[44] is also used, it reads:

$$\Lambda = 0.42 L_{\mathrm{w}}. \tag{30}$$

u_{rms} is obtained using the turbulent kinetic energy definition formula for homogeneous turbulence:[43]

$$u_{rms} = \sqrt{\frac{2}{3}k}. \tag{31}$$

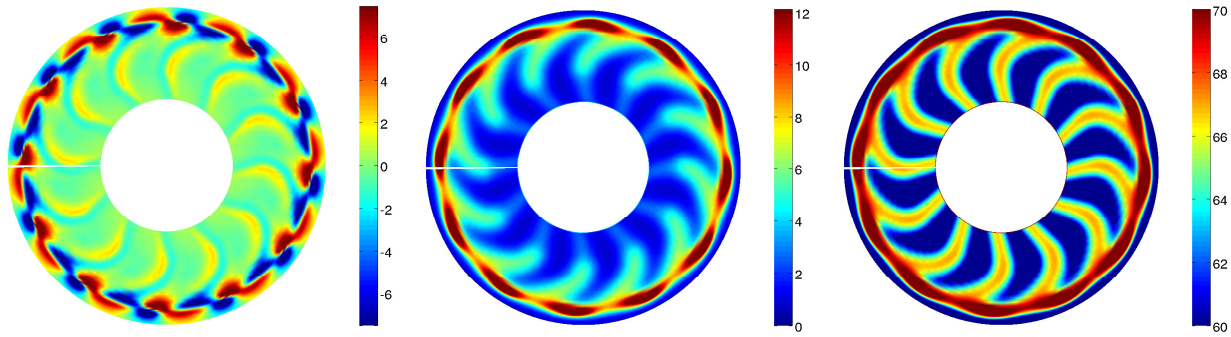

(a) Axial velocity fluctuations $[m/s]$

(b) Turbulent kinetic energy (k) $[m^2/s^2]$

(c) $10\log$(Specific dissipation (ω)) $[1/s]$

Figure 15: Raw CFD inputs maps for the turbulent velocity wake reconstruction. Plane extracted at constant distance from the aft rotor leading edge following the approach described in Carazo.[17]

On the one hand, Figure 16a shows that the half-wake size using the axial velocity fluctuation has large fluctuations, especially at high radii. These fluctuations are caused by the presence of the tip-vortex which does not behave as a classical viscous wake. This indicates that maybe a dedicated tip-vortex broadband model should be investigated in the future in order to correctly model the broadband noise created by the impingement of turbulent vortices of rotating blades. On the other hand, it appears that Λ is correctly predicted using the turbulent variables and is going to be used for further computations. Figure 16b shows the Von Karman spectra for different radial positions. The intensity of the turbulence increases along the radius and reach its maximum at the tip vortex location.

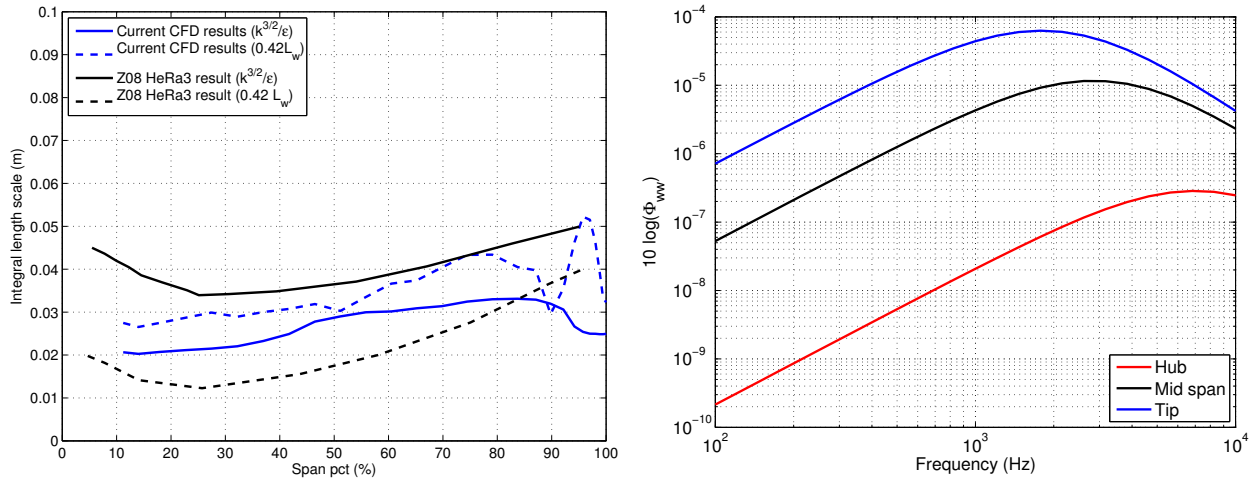

(a) Integral length scale.

(b) $\Phi^{(2)}_{ww}$ for different strips.

Figure 16: Comparison of the integral length scale and Von Karman spectra for different radii. HeRa 3 values coming from Nodé-Langlois *et al.*[45]

Now that the velocity inputs are set, the final formulation of the acoustic pressure density can be described.

Figure 17a shows the directivity of the BRWI model for different frequencies. The maximum of the power spectra is located at the same frequency than the velocity spectra for the tip strip indicating that the BRWI for this case is tip-driven. This is confirmed by the power level results of the geometry presented in Figure 17b indicating that the tip is the main contributor for BRWI mechanism. However, the wake approach described by Blandeau *et al.*[2] may be inadequate for a Broadband Rotor-Vortex Interaction (BRVI) modeling, however

this needs to be confirmed with experiments. In fact, the modulation function f_{w} may be changed in a further work in order to take into account the particular case of tip-vortices.

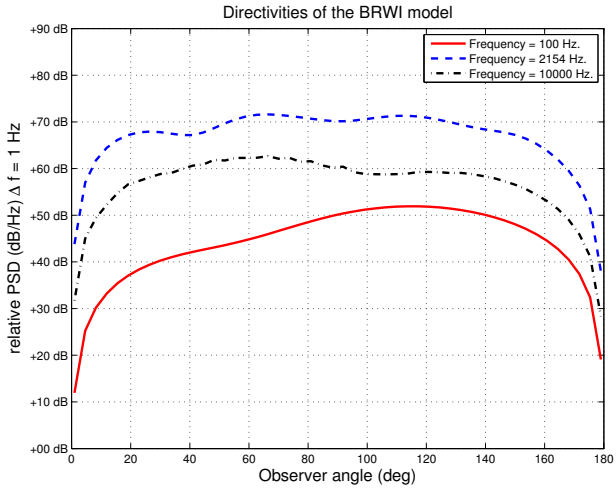

(a) BRWI directivites.

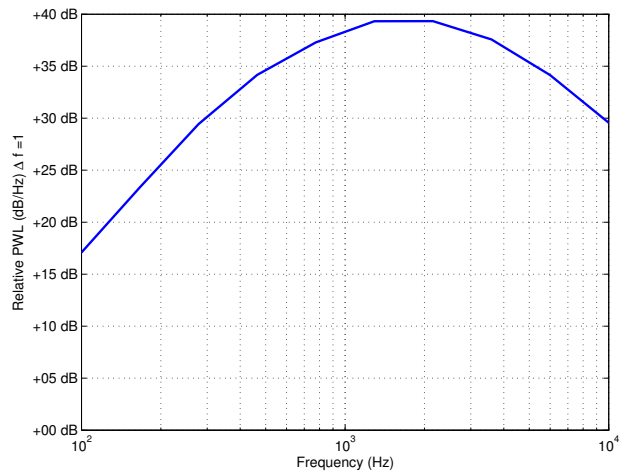

(b) Power spectrum of the configuration.

Figure 17: Acoustic results for the BRWI model on the current CROR geometry. $\Delta f = 1$.

IV. Conclusions

To conclude, a preliminary CROR semi-empirical approach for both tonal and broadband noise was drawn. For the moment, it consists in a tonal vortex model coupled with a broadband wake-blade model. On the one hand, several modifications can be performed for the OBVI model in order to evaluate correctly the effect of the tip which seems to largely modifies the response on the blade. On the other hand the sensitivity of the acoustic sources was performed and the MCS showed better results when compared with a classical flat plate approach.

Concerning the BRWI, the implementation was validated using a canonical geometry. It was applied to a modern CROR geometry showing that the BRWI noise is largely tip-driven for this geometry and operating point. This is due to the presence of a highly turbulent tip-vortex. However, the half-wake size used in the model in order to represent the periodic impingement of turbulent wakes seems inadequate for the BRVI mechanism, since a Gaussian formulation cannot described the geometrical features of a vortex. However comparisons with experiments are required in order to confirm the necessity of a modified BRVI model. Modified dimensionless modulation functions need investigation taking into account the particular case of vortices as turbulent sources.

References

[1]Quaglia, M. E., Moreau, S., Roger, M., and Fernando, R., "A three-dimensional analytical approach for Open-Rotor Blade Vortex Interaction (BVI) tonal noise," in the 21th AIAA/CEAS Aeroacoustics Conference, Dallas, Texas, USA, 22-26 June, 2015, pp. 2015–2984.

[2]Blandeau, V., Joseph, P., Kingan, M., and Parry, A., "Broadband noise predictions from uninstalled contra-rotating open rotors," *International Journal of Aeroacoustics*, Vol. 12, No. 3, 2013, pp. 245–282.

[3]Carazo, A., Roger, M., and Omais, M., "Analytical prediction of wake-interaction noise in counter-rotation open rotors," in the 17th AIAA/CEAS Aeroacoustics Conference, Portland, Oregon, USA, 5-8 June, 2011.

[4]Gordon, E. and Woodward, R., "Noise of a model counterrotation propeller with reduced aft rotor diameter at simulated takeoff/approach conditions (F7/A3)," *AIAA Paper 88-0263*.

[5]Fernando, R. and Leroux, M., "Open-Rotor low speed aero-acoustics: wind tunnel characterization of an advanced blade design in isolated and installed configurations," in the 20th AIAA/CEAS Aeroacoustics Conference, Atlanta, GA, USA, 16-20 June, 2014.

[6]Lepot, I., Leborgne, M., Schnell, R., Yin, J., Delattre, G., Falissard, F., and Talbotec, J., "Aero-mechanical optimization of a contra-rotating open rotor and assessment of its aerodynamic and acoustic characteristics," *Proceedings of the Institution of Mechanical Engineers, Part A: Journal of Power and Energy*, Vol. 225, No. 7, 2011, pp. 850–863.

[7]Schnell, R., Yin, J., Voss, C., and Nicke, E., "Assessment and optimization of the aerodynamic and acoustic characteristics of a counter rotating open rotor," *Journal of Turbomachinery*, Vol. 134, No. 6.

[8]Peters, A. and Spakovszky, Z. S., "Rotor interaction noise in counterrotating propfan propulsion systems," *Journal of Turbomachinery*, Vol. 134, No. 1, 2012, p. 011002.

[9]Parry, A., Kingan, M., and Tester, B., "Relative importance of open rotor tone and broadband noise sources," in the 17th AIAA/CEAS Aeroacoustics Conference, Portland, Oregon, USA, 5-8 June, 2011, pp. 5–8.

[10]Parry, A. B., "Theoretical prediction of counter-rotating propeller noise," Phd. thesis, University of Leeds, Leeds, UK, 1988.

[11]Jaouani, N., Roger, M., Nodé-Langlois, T., and Serre, G., "Analytical Prediction of the Pylon-Wake Effect on the Tonal Noise Radiated by the Front Rotor of CROR Propulsion Systems," in the 21th AIAA/CEAS Aeroacoustics Conference, Dallas, Texas, USA, 22-26 June, 2015, pp. 2015–2985.

[12]Majjigi, R., Uenishi, K., and Gliebe, P., "An investigation of counterrotating tip vortex interaction," *NASA CR-185135*.

[13]Jaron, R., Moreau, A., and Guérin, S., "Extrapolation of RANS flow data for improved analytical fan tone prediction," in the 21th AIAA/CEAS Aeroacoustics Conference, Dallas, Texas, USA, 22-26 June, 2015, pp. 2015–2515.

[14]Soulat, L., Kernemp, I., Sanjose, M., Moreau, S., and Fernando, R., "Assessment and comparison of tonal noise models for Counter-Rotating Open Rotors," in the 19th AIAA/CEAS Aeroacoustics Conference, Berlin, Germany, 27-29 May, 2013, pp. 2013–2201.

[15]Roger, M., Schram, C., and Moreau, S., "On vortex–airfoil interaction noise including span-end effects, with application to open-rotor aeroacoustics," *Journal of Sound and Vibration*, Vol. 333, No. 1, 2014, pp. 283–306.

[16]Hanson, D. B. and Parzych, D. J., "Theory for noise of propellers in angular inflow with parametric studies and experimental verification," *NASA-CR-4499*.

[17]Carazo, A., "Semi-analytical prediction of wake-interaction noise in counter-rotating open rotors," Phd. thesis, Ecole Centrale de Lyon, Lyon, France, 2012.

[18]Blandeau, V., "Aerodynamic broadband noise from contra-rotating open rotors," Phd. thesis, University of Southampton, Southampton, UK, 2011.

[19]Kingan, M. J., "Open rotor broadband interaction noise," *Journal of Sound and Vibration*, Vol. 332, No. 17, 2013, pp. 3956–3970.

[20]Fedala, D., "Modélisation du bruit à large bande rayonné par un profil isolé: application aux turbomachines," Phd. thesis, ParisTech, Paris, France, 2007.

[21]Van Zante, D. E. and Wernet, M. P., "Tip vortex and wake characteristics of a counterrotating open rotor," in Proceedings of the 48th AIAA/ASME/SAE/ASEE Joint Propulsion Conference & Exhibit. AIAAVol. 4039, 2012.

[22]Kok, J. C., "Resolving the dependence on freestream values for the k-turbulence model," *AIAA journal*, Vol. 38, No. 7, 2000, pp. 1292–1295.

[23]Menter, F. R., "Zonal two equation k-turbulence models for aerodynamic flows," *AIAA paper*, Vol. 2906, 1993, p. 1993.

[24]Liou, M.-S., "A sequel to ausm: Ausm+," *Journal of computational Physics*, Vol. 129, No. 2, 1996, pp. 364–382.

[25]Soulat, L., Kernemp, I., and Fernando, R., "Numerical assessment of noise emission of counter-rotating open rotors," in the 10th European Turbomachinery Conference, Lappeerenta, Finland, 2013.

[26]Jeong, J. and Hussain, F., "On the identification of a vortex," *Journal of fluid mechanics*, Vol. 285, 1995, pp. 69–94.

[27]Strawn, R. C., Kenwright, D. N., and Ahmad, J., "Computer visualization of vortex wake systems," *AIAA journal*, Vol. 37, No. 4, 1999, pp. 511–512.

[28]Fabre, D., "Instabilité et instationnarités dans les tourbillons: Application aux sillages d'avions," Phd. thesis, Universite Paris VI, Paris, France, 2002.

[29]Falissard, F. and Delattre, G., "Investigation of Counter-Rotating Open-Rotor Orthogonal Blade/Vortex Interaction Noise," in the 20th AIAA/CEAS Aeroacoustics Conference, Atlanta, GA, USA, 16-20 June, 2014.

[30]Delattre, G. and Falissard, F., "Influence of Torque Ratio on Counter-Rotating Open-Rotor Interaction Noise," in the 20th AIAA/CEAS Aeroacoustics Conference, Atlanta, GA, USA, 16-20 June, 2014.

[31]Amiet, R. K., "High frequency thin-airfoil theory for subsonic flow," *AIAA Journal*, Vol. 14, No. 8, 1976, pp. 1076–1082.

[32]Christophe, J., "Application of hybrid methods to high frequency aeroacoustics," Phd. thesis, von Karman Institute for Fluid Dynamics, Bruxelles, Belgium, 2011.

[33]Roger, M. and Carazo, A., "Blade-geometry considerations in analytical gust-airfoil interaction noise models," in the 16th AIAA/CEAS Aeroacoustics Conference, Stockholm, Sweden, May, 2010.

[34]Roger, M. and Moreau, S., "Back-scattering correction and further extensions of Amiet's trailing-edge noise model. Part 1: theory," *Journal of Sound and Vibration*, Vol. 286, No. 3, 2005, pp. 477–506.

[35]Falissard, F., Zehner, P., Roger, M., and Gloerfelt, X., "Numerical and Analytical Investigation of Orthogonal Blade/Vortex Interaction Noise," in the 21th AIAA/CEAS Aeroacoustics Conference, Dallas, Texas, USA, 22-26 June, 2015, p. 2843.

[36]Vion, L., Delattre, G., Falissard, F., and Jacquin, L., "Counter-Rotating Open Rotor (CROR): flow physics and simulation," *20ème Congrès Français de Mécanique, Besancon, France, 28 aout/2 sept.*

[37]Giez, J., Vion, L., and Roger, S., Michel andMoreau, "Effect of the Edge-and-Tip Vortex on Airfoil Selfnoise and Turbulence Impingement Noise," in the 22th AIAA/CEAS Aeroacoustics Conference, Lyon, France, 30 May - 1 June, 2016.

[38]Casalino, D., "An advanced time approach for acoustic analogy predictions," *Journal of Sound and Vibration*, Vol. 261, No. 4, 2003, pp. 583–612.

[39]Amiet, R., "Acoustic radiation from an airfoil in a turbulent stream," *Journal of Sound and vibration*, Vol. 41, No. 4, 1975, pp. 407–420.

[40]Amiet, R. K., "Compressibility effects in unsteady thin-airfoil theory," *AIAA Journal*, Vol. 12, No. 2, 1974, pp. 252–255.

[41]Ventres, C., Theobald, M., and Mark, W. D., "Turbofan noise generation. volume 1: Analysis," *NASA STI/Recon Technical Report N*, Vol. 83, 1982, p. 15041.

[42]Nallasamy, M. and Envia, E., "Computation of rotor wake turbulence noise," *Journal of Sound and Vibration*, Vol. 282, No. 3, 2005, pp. 649–678.

[43]Pope, S. B., "Turbulent Flows," *Turbulent Flows, by Stephen B. Pope, pp. 806. ISBN 0521591252. Cambridge, UK: Cambridge University Press, September 2000.*, p. 806.

[44]Jurdic, V., Joseph, P., and Antoni, J., "Investigation of rotor wake turbulence through cyclostationary spectral analysis," *AIAA Journal*, Vol. 47, No. 9, 2009, pp. 2022–2030.

[45]Nodé-Langlois, T., Wlassow, F., Languille, V., Colin, Y., Caruelle, B., Gill, J., Chen, X., Zhang, X., and Parry, A., "Prediction of Contra-Rotating Open Rotor broadband noise in isolated and installed configurations," in the 20th AIAA/CEAS Aeroacoustics Conference, Atlanta, GA, USA, 16-20 June, 2014.